

# JGR Earth Surface

## RESEARCH ARTICLE

10.1029/2020JF005930

# Revealing the Importance of Capillary and Collisional Stresses on Soil Bed Erosion Induced by Debris Flows

Pengjia Song<sup>1</sup>  and Clarence Edward Choi<sup>1</sup> 

<sup>1</sup>Department of Civil Engineering, The University of Hong Kong, Pok Fu Lam, Hong Kong SAR, China

### Key Points:

- Soil bed erosion by debris flow exhibits a parabola-like relationship with bed water content under the influence of capillary stresses
- Basal collisional stresses have been largely ignored but are a major contributing factor to soil bed erosion by debris flow
- The effects of capillary and collisional stresses need to be captured in debris flow models to improve hazard delineation

### Correspondence to:

C. E. Choi,  
cechoi@hku.hk

### Citation:

Song, P., & Choi, C. E. (2021). Revealing the importance of capillary and collisional stresses on soil bed erosion induced by debris flows. *Journal of Geophysical Research: Earth Surface*, 126, e2020JF005930. <https://doi.org/10.1029/2020JF005930>

Received 4 OCT 2020  
Accepted 28 APR 2021

**Abstract** Climate change is increasing the frequency of extreme rainfall events and the snow cover to melt at high altitudes, which may exacerbate the threat posed by debris flows. Soil bed erosion, the process by which the bed material fails under loadings from a debris flow, is perhaps the most important momentum exchange process that governs the destructive potential of debris flows. Existing erosion theories adopt saturated soil mechanics to describe the failure of soil bed and place a strong emphasis on the basal friction induced shear stress as the driving mechanism. However, soil beds in nature are rarely saturated and field observations have hinted at the importance of collisional stresses as a driving mechanism. In this study, an unsaturated soil mechanics framework is used to characterize soil bed erosion by collisional flows. Experiments were conducted to model the erosion of unsaturated sandy beds with a wide range of initial matric suction values, which is a measure of capillary stresses, by gravel flows. Contrary to the existing literature, the rate of erosion does not increase linearly but demonstrates a parabola-like relationship with the bed water content because the shear strength of unsaturated soil is governed by capillary stresses. The importance of collisional stresses on soil bed erosion is demonstrated by a newly proposed dimensionless number. Findings indicate that existing erosion models largely underestimate channel bed erosion, especially for soil beds with low water content, and stress the importance of hydro-mechanical coupling to advance the current state of debris flow hazard delineation.

## 1. Introduction

Debris flows (Hungri et al., 2014) surge downslope at high velocities under the influence of gravity. Such flows may cause fatalities (Froude & Petley, 2018) and damage to infrastructure (Jakob et al., 2012). The destructive potential of these flows is enhanced by their ability to erode bed material along their flow paths (Hungri et al., 2005). Thus, reliable predictions of erosion are central to the delineation of debris flow hazards. Despite a multitude of erosion models proposed in the literature (Cao et al., 2004; Fraccarollo & Capart, 2002; McDougall & Hungri, 2005; Medina et al., 2008; Pirulli & Pastor, 2012; Sovilla et al., 2006; Sutherland, 1967; Takahashi, 1978), erosion remains one of the most difficult momentum exchange processes to predict (Hungri et al., 2005; Iverson, 2012). Thus, fundamental research is essential to improve our understanding of the erosion process.

Unique measurements of debris flows in Switzerland suggest that coarse particles at the flow front (Figure 1a) generate high collisional stresses (McArdell et al., 2007) and that soil bed erosion predominantly occurs during the passage of the collisional flow front (Berger et al., 2011). More interestingly, the basal shear stress measured by the force plate (Figure 1b) remains nearly constant as the debris flow passes over it (Berger et al., 2011), and the strength of the soil bed estimated from the reported data is higher than the basal shear stress measured by the force plate when erosion occurs. These field observations hint at the conjecture that basal friction induced shear stress is not the only driving mechanism causing soil bed erosion. In fact, collisional stresses may also play a significant role in erosion by imposing large point loads on the soil beds (Figure 1c). Collisional stresses generated by coarse particles have been reported to cause bedrock erosion (Stock & Dietrich, 2003). Given that bedrock is significantly stronger than soil, it is reasonable to assume that the grain collisional stresses should play a dominant role in soil bed erosion as well.

Another common idealization made in the theoretical representation of soil bed erosion is that saturated soil mechanics (Terzaghi, 1936) can describe the failure of the soil bed. However, channel beds are seldom fully saturated in nature when debris flows occur (McCoy et al., 2012). A strong foundation of work in unsaturated soil mechanics has shown that capillary stresses due to the presence of air-water interfaces

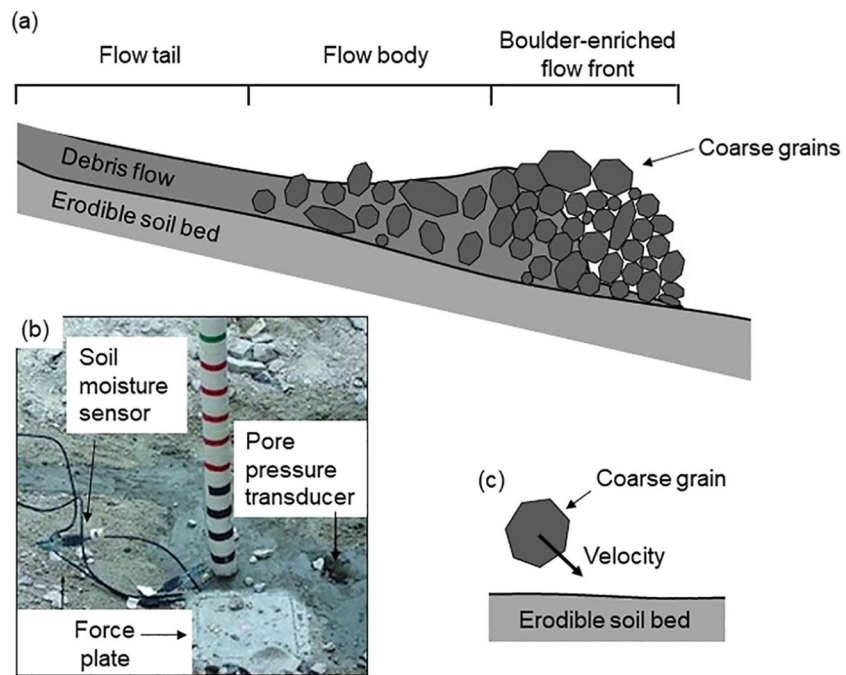


**Figure 1.** Conceptual figures. (a) Typical structure of a debris flow; (b) Instrumentation including a force plate, a soil moisture sensor and a pore pressure transducer installed at the field observation station at the Chalk Cliff, USA (McCoy et al., 2012), (photo is used by permission of the *Journal of Geophysical Research: Earth Surface*); (c) Point loads induced by basal collisional stresses of the flow on soil bed.

significantly contribute to the shear strength (Fredlund et al., 1978). The peak shear strength of unsaturated soil has been reported to be up to three times larger than that at its saturated state (Fredlund et al., 1996; Vanapalli et al., 1996). Furthermore, in saturated soils, any external undrained loading is directly transferred to the pore water (Skempton, 1954). However, for unsaturated soils, the compressibility of pore air affects the transfer of undrained loading to the soil bed (Hasan & Fredlund, 1980).

In this study, we propose a new theory on soil bed erosion based on unsaturated soil mechanics and the assumption that soil bed erosion is driven by collisional stresses. A series of unique experiments were carried out to evaluate the proposed theory. Dry gravels are used to model flows that are dominated by collisional stresses to mimic the flow front of a natural debris flow. The water content of the soil beds was varied in the experiments to study the effects of matric suction, which is a measure of capillary stresses, on soil bed erosion caused by flows dominated by collisional stresses.

## 2. Theoretical Analysis of Erosion of Unsaturated Soil Bed by Collisional Flows

Soil bed erosion is the failure of the soil bed material under the influence of external stresses. The core of any theoretical representation of soil bed erosion requires the characterization of the dominate driving and resisting mechanisms. In this section, the driving mechanism (i.e., basal collisional stresses) and the resisting mechanism (i.e., unsaturated soil bed strength) are characterized.

### 2.1. Erosion of Soil Bed Caused by Collisional Stresses

Revealing the dominant driving mechanism of soil bed erosion is central to elucidating the underlying mechanism of erosion. Field observations show that collisional stresses at the base of a flow may drive erosion by generating point loads that are as high as 10 MPa (Okuda et al., 1980). Such loads are sufficient to cause soil bed failure, which leads to erosion. The magnitude of the point loads is proportional to the

collisional stresses, which is as follows (Hsu et al, 2008, 2014; Stock & Dietrich, 2006; Yohannes et al., 2012) defined by Bagnold (1954):

$$\sigma_i = v_s \rho_s D_e^2 \dot{\gamma}^2 \quad (1)$$

where  $v_s$  is the solid fraction of the debris flow,  $\rho_s$  and  $D_e$  are the density and characteristic grain diameter of the solid particles, respectively, and  $\dot{\gamma}$  is the shear rate near the flow base. Thus, the erosion rate of soil beds by collisional stresses is proposed to be proportional to the strength normalized collisional stress  $N_{\text{SNCS}}$ , which is defined as the ratio of the basal collisional stresses to the shear strength of the soil bed:

$$-\frac{\partial z}{\partial t} = K \cdot N_{\text{SNCS}} \quad (2a)$$

$$N_{\text{SNCS}} = \frac{v_s \rho_s D_e^2 \dot{\gamma}^2}{\tau_f} \quad (2b)$$

where  $K$  is a coefficient related to the properties of the flow material and may be interpreted as the ratio of the stress from point loads imposed on the soil beds to the collisional stresses defined by Bagnold (1954). Since the magnitude of point loads, which causes soil bed failure, cannot be directly measured, it is expressed as the product of the collisional stresses and a proportionality coefficient.  $\tau_f$  is the shear strength of the soil bed at failure. Equation 2 was originally proposed to estimate the erosion of bedrock by collisional flows (Stock & Dietrich, 2006), where the erosion rate was reported to exhibit a linear relationship with  $N_{\text{SNCS}}$ . However, the failure mechanisms for soil and rock are different. For soil beds, failure occurs when the induced shear stress exceeds the shear strength of the soil (Terzaghi, 1936). After which, the soil particles will slide along a failure plane. In contrast, rock beds fail by tensile failure, which is initiated at discontinuities (Jaeger et al., 2009). Thus, the denominator of  $N_{\text{SNCS}}$  needs to be modified to cater for soil.

## 2.2. The Shear Strength of Unsaturated Soils

Since soil beds in nature are rarely saturated, unsaturated soil mechanics is required to yield a more accurate estimation of the bed shear strength, which in turn improves predictions of the erosion of soil beds. In this section, we first present the shear strength equation for unsaturated soils, followed by the influence of undrained loading on the shear strength of unsaturated soils. Then, the influence of bed water content on the unsaturated shear strength is discussed.

### 2.2.1. The Initial Strength of Unsaturated Soil Bed

The stress state parameters governing the shear strength of saturated and partially saturated soils are different. The shear strength of saturated soils is governed by a single stress state parameter, namely, the effective stress ( $\sigma_n - u_w$ ), where  $\sigma_n$  and  $u_w$  are the normal stress and pore water pressure, respectively. The pore water pressure in saturated soil generally has a positive value (Terzaghi, 1936). Any increase in pore water pressure will push soil particles apart and reduce the shear strength of the soil (Terzaghi, 1936). However, air flows into the voids when the soil desaturates. The voids and soil skeleton enable capillary action, whereby air-water interfaces called contractile skins act as elastic membranes to hold soil particles together via surface tension (Fredlund & Morgenstern, 1978). Furthermore, capillary effects result in a negative pore water pressure when referenced to the atmospheric pressure (Fredlund & Morgenstern, 1978). Unlike a positive pore water pressure, a negative pore water pressure in unsaturated soils tends to hold soil particles together. The surface tension exerted by the contractile skins and the negative pore water pressure provide additional shear resistance for unsaturated soils (Fredlund et al., 1978; Lu, 2008). The shear strength of unsaturated soils can be expressed as follows (Fredlund et al., 1978; Lu, 2008):

$$\tau = (\sigma_n - u_a) \tan \phi' + (u_a - u_w) \tan \phi^b \quad (3)$$

where  $u_a$  and  $u_w$  are the pore air pressure and pore water pressure, respectively,  $\phi'$  is the internal friction angle of the soil and  $\tan \phi^b$  quantifies the effect of the matric suction ( $u_a - u_w$ ) on the shear strength.

Equation 3 shows that the shear strength of unsaturated soils is governed by two stress state parameters, specifically the net normal stress ( $\sigma_n - u_a$ ) and the matric suction ( $u_a - u_w$ ).

### 2.2.2. Influence of Undrained Loading on the Shear Strength of Unsaturated Soil Beds at Failure

Debris flows travel at high speeds and impose rapid loading on soil beds (Hung et al., 2014; Takahashi, 1978). Rapid loading influences the shear strength of unsaturated soil beds by inducing changes in pore pressure (Skempton, 1954). If the rate of loading is higher than that at which the pore fluid drains from the soil matrix, then the loading is considered undrained and the pore pressure will increase. The increase in pore pressure will decrease the strength of the soil (Atkinson, 2007). Furthermore, the normal stress, instead of the shear stress, induced by a debris flow on a soil bed is responsible for generating high excess pore pressure during undrained loading. Thus, the response of the pore air pressure and pore water pressure to external loading can be calculated as follows (Skempton, 1954):

$$\Delta u_a = B_a \cdot \Delta \sigma \quad (4a)$$

$$\Delta u_w = B_w \cdot \Delta \sigma \quad (4b)$$

where  $\Delta \sigma$  is the incremental normal stress,  $B_a$  and  $B_w$  are the pore air pressure parameter and pore water pressure parameter, respectively.

Pore pressure parameters are inversely proportional to the ratio of the compressibility of the pore fluid to the compressibility of the soil skeleton (Bishop, 1954; Skempton, 1954). In saturated soils, the pore water pressure parameter is assumed to be unity because the compressibility of the pore water is relatively low compared to that of the soil skeleton (Hasan & Fredlund, 1980; Skempton, 1954). However, in unsaturated soils, the high compressibility of the pore air renders increases in both the pore water pressure and pore air pressure smaller than the external loading. More specifically, both  $B_a$  and  $B_w$  are smaller than unity (Hasan & Fredlund, 1980). For unsaturated soils subjected to undrained loading, the pore pressure parameters can be expressed as follows (Hilf, 1948):

$$B_a = B_w = 1 / \left[ 1 + \frac{(1 - S_0)n_0}{m_v(u_{a0} + \Delta u_a)} \right] \quad (5)$$

where  $S_0$  and  $n_0$  are the initial degree of saturation and initial void ratio of the soil, respectively,  $m_v$  is the compressibility of the soil obtained from an odometer test,  $u_{a0}$  is the initial pore air pressure and  $\Delta u_a$  is the incremental pore air pressure.

If the pore air pressure is assumed to be atmospheric, then the pore pressure during undrained loading can be calculated as follows:

$$u_a = B_a \cdot \Delta \sigma \quad (6a)$$

$$u_w = -(u_a - u_w)_0 + B_w \cdot \Delta \sigma \quad (6b)$$

where  $(u_a - u_w)_0$  is the initial matric suction. Equation 6b can then be used to explain why positive pore water pressure is more readily generated for soil beds with a higher bed water content, as observed by Iverson et al. (2011) (to be discussed in Section 5).

The change in the pore pressure during undrained loading results in a change in the shear strength of the unsaturated soil. By substituting Equation 6 into Equation 3, the shear strength of an unsaturated soil bed undergoing undrained loading  $\tau_f$  can be expressed as follows:

$$\tau_f = \sigma_n \tan \phi' + (u_a - u_w)_0 \tan \phi^b - B_a \sigma_n \tan \phi' \quad (7)$$

Equation 7 can then be substituted into Equation 2 to estimate the erosion rate of an unsaturated soil bed subjected to collisional stresses:

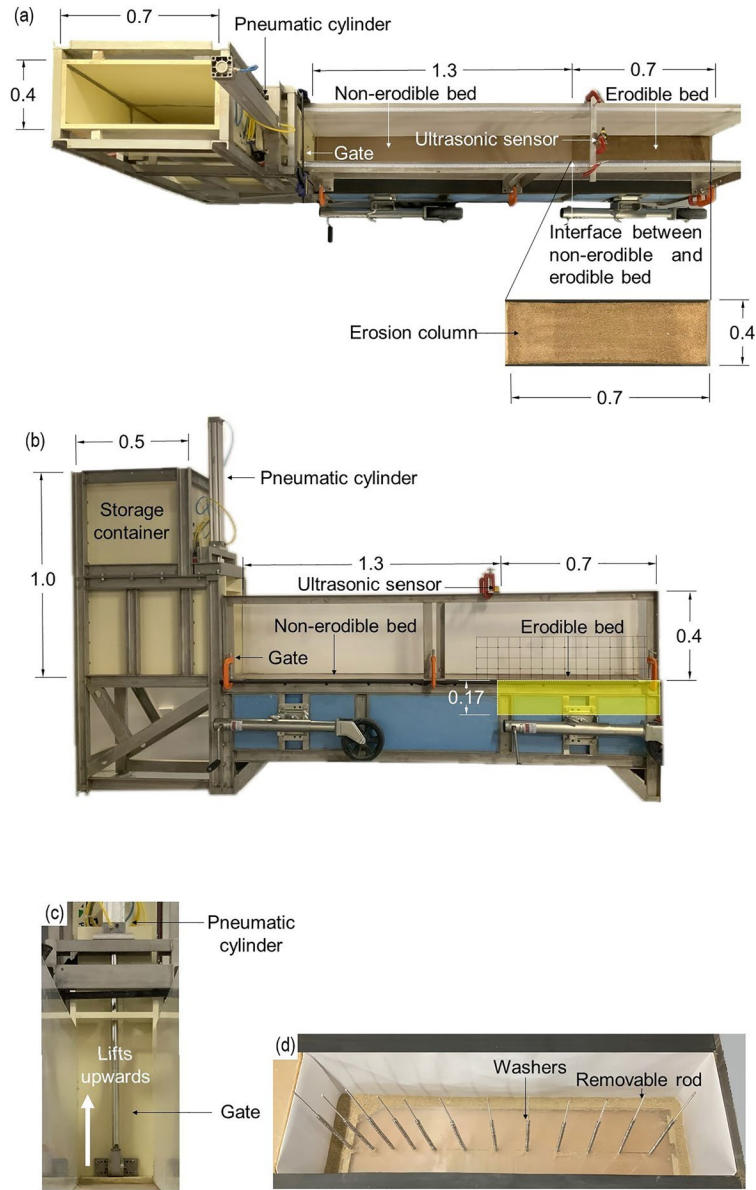


**Figure 2.** Experimental setup. (a) Side view of the flume; (b) Top view of the flume; (c) Front view of the pneumatically controlled gate; (d) Top view of the erodible section with erosion columns without soil. All dimensions are in meter. The Pneumatically controlled gate lifts vertically to simulate dam-break during each experiment.

$$-\frac{\partial z}{\partial t} = K \cdot N_{\text{SNCS}} \quad (8a)$$

$$N_{\text{SNCS}} = \frac{v_s \rho_s D_e^2 \dot{\gamma}^2}{\sigma_n \tan \phi' \phi + (u_a - u_w)_0 \tan \phi^b - B_a \sigma_n \tan \phi'} \quad (8b)$$

### 2.2.3. Variation of Shear Strength of Unsaturated Soil Bed with Bed Water Content

The shear strength of unsaturated soil is significantly influenced by the water content, which governs the matric suction. Understanding the relationship between the unsaturated shear strength of the soil and its water content is critical to reveal the influence of bed water content on soil bed erosion. With decreasing water content, the matric suction increases, however,  $\tan \phi^b$  decreases from  $\tan \phi'$  to 0 (Vanapalli et al., 1996).

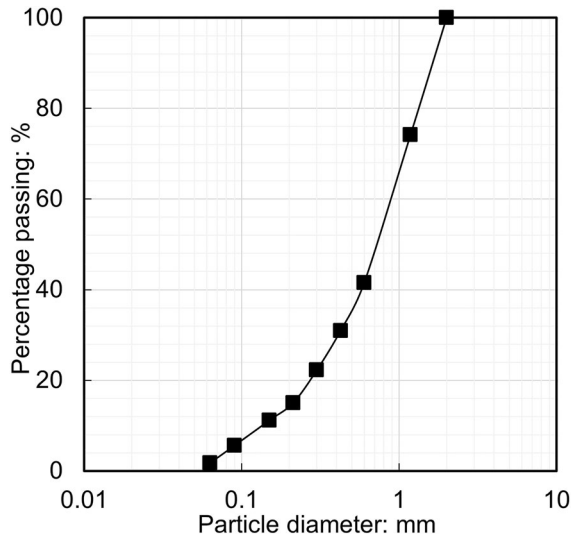


**Figure 3.** The particle size distribution of the soil bed material. The vertical axis represents the mass percentage of the soil particles passing the sieve with a specific mesh size.

The reduction in  $\tan\phi^b$  is because both the contact area of the solid-water interfaces, which quantifies the influence of the negative pore water pressure on shear strength, and the quantity of the contractile skins, which quantifies the influence of the surface tension exerted by the contractile skins on the shear strength, decrease with the water content (Lu, 2008; Lu & Likos, 2006). Thus, at a saturated state,  $(u_a - u_w) = 0$  and  $\tan\phi^b = \tan\phi'$ , the shear strength of the soil can be captured by using classical shear strength theory for saturated soils (Terzaghi, 1936). However, when a soil desaturates, the shear strength increases until a peak value is reached. With a further decrease in the water content, the shear strength decreases to that of a dry soil, where  $\tan\phi^b = 0$  (Fredlund et al., 1996; Gan et al., 1988). Thus, the initial shear strength of the soil bed (Equation 3) increases with the water content until a peak value is reached and then decreases with the water content.

Apart from influencing the initial shear strength, the bed water content also affects the shear strength of soil beds at failure by varying the pore pressure increase during undrained loading. Both  $B_a$  and  $B_w$  decrease with water content (Equation 5). A smaller  $B_a$  and  $B_w$  results in a smaller increase in both pore air pressure and pore water pressure (Equation 4), and a smaller decrease in the shear strength (Equation 7) during undrained loading.

### 3. Physical Modeling of Erosion of Unsaturated Soil Bed by Gravel Flows

#### 3.1. Scaling Considerations

In this study, flume experiments were conducted to evaluate the effects of capillary and collisional stresses on the erosion of an unsaturated soil bed. Scaling considerations in the design of the flume experiments ensure that the lab-scale experiment results will have relevance to real debris flow events. Field observations report that the front of a debris flow can be characterized as a permeable assembly of coarse grains that sustain little to no excess pore fluid pressure (Iverson, 1997). Thus, the viscous stress caused by the interstitial fluid is negligible compared to the large collisional inter-particle stresses generated by the coarse

**Table 1**  
Summary of Experimental Program and Bed Properties

Test ID	Bed material properties					
	Dry density, $\rho_d$ (kg/m <sup>3</sup> )	Void ratio, $n$	Volumetric water content, $\theta$	Initial matric suction, $(u_a - u_w)_0$ (kPa)	Pore pressure parameter, $B$	Shear strength at failure, $\tau_f$ (kPa)
$\theta_0$	1,305	1.01	0.00	-	0.48	0.62
$\theta_{006}$	1,307	1.00	0.06	97.8	0.51	1.10
$\theta_{011}$	1,315	0.99	0.11	79.5	0.54	5.60
$\theta_{013}$	1,329	0.97	0.13	68.0	0.55	7.38
$\theta_{016}$	1,319	0.99	0.16	26.0	0.58	6.74
$\theta_{018a}$	1,319	0.99	0.18	14.0	0.59	4.12
$\theta_{018b}$	1,310	1.00	0.18	10.8	0.59	3.24
$\theta_{020}$	1,339	0.96	0.20	5.0	0.60	1.93
$\theta_{021}$	1,327	0.97	0.21	1.7	0.61	0.95
$\theta_{022}$	1,329	0.97	0.22	1.3	0.63	0.85
$\theta_{024}$	1,323	0.98	0.24	0.9	0.64	0.71
$\theta_{028}$	1,329	0.97	0.28	0.4	0.68	0.53
$\theta_{030}$	1,340	0.96	0.30	0.1	0.71	0.37

**Table 2**  
Summary of Flow and Erosion Data

Test ID	Flow dynamic properties			Erosion data	
	Basal shear rate, $\dot{\gamma}$ (1/s)	Savage number, $N_{Sav}$	Strength normalized collisional stress, $N_{SNCs}$	Erosion depth, $e$ ( $10^{-3}$ m)	Erosion rate, $\dot{e}$ ( $10^{-3}$ m/s)
$\theta_0$	50.47	0.37	0.89	32.06	13.98
$\theta_{006}$	53.50	0.42	0.57	24.22	10.19
$\theta_{011}$	51.09	0.38	0.10	13.15	3.50
$\theta_{013}$	55.49	0.45	0.09	9.94	2.96
$\theta_{016}$	47.35	0.33	0.07	5.82	1.68
$\theta_{018a}$	50.20	0.37	0.13	10.64	3.04
$\theta_{018b}$	43.11	0.27	0.12	6.90	2.42
$\theta_{020}$	49.00	0.35	0.27	7.06	3.22
$\theta_{021}$	43.18	0.27	0.43	8.60	4.39
$\theta_{022}$	43.34	0.28	0.48	10.33	5.13
$\theta_{024}$	42.55	0.27	0.55	13.15	7.58
$\theta_{028}$	45.38	0.30	0.85	18.82	13.02
$\theta_{030}$	41.51	0.25	1.03	23.38	16.17

grains typically observed at the front of a debris flow (Iverson, 1997; McArdell et al., 2007). Mesoscopic scaling was adopted to achieve dynamic similarity between the model flows and the flow front of a natural debris flow. This type of scaling considers the grain-scale interactions, which ultimately gives rise to the macroscopic behavior of a debris flow (Iverson, 1997). The Savage number  $N_{Sav}$ , which characterizes the relative importance between collisional and frictional inter-particle stresses, is the most relevant dimensionless number for scaling the collisional flow fronts in this study:

$$N_{Sav} = \frac{v_s \rho_s D_e^2 \dot{\gamma}^2}{\rho g h \tan \phi'} \quad (9)$$

where  $\rho$  is the bulk density of the flow,  $h$  is the flow depth and  $\phi'$  is the effective friction angle of the solid grains in the flow. The numerator of the right side of Equation 9 represents the characteristic collisional stresses of the flow and the denominator represents the frictional stress of the flow. The inter-particle collisional stresses dominate the interaction of solid grains when the Savage number  $N_{Sav}$  is greater than 0.1 (Savage & Hutter, 1989). The configuration of the experimental setup was selected based on the aforementioned scaling considerations (to be discussed in Section 3.2).

### 3.2. Experimental Setup

The flume model used in this study adopts a typical configuration for studying soil bed erosion (Estep & Dufek, 2012; Haas & Woerkom, 2016; Wu et al., 2018). The flume is 2 m in length and was developed specifically for this study (Figure 2). The channel width is 0.2 m. The channel bed has a 1.3-m long smooth non-erodible section, followed by a 0.7-m long erodible section. The transition from a rigid to an erodible section in the flume can be idealized as the transition from a rock bed to an erodible soil one in a natural channel (Haas & Woerkom, 2016). During each test, a mass of gravel with an initial depth  $h_0$  of 0.48 m and a width  $r_0$  of 0.5 m (i.e., an aspect ratio  $h_0/r_0$  of 0.96) was prepared in the storage container, which is located at the upper end of the flume model. It is acknowledged that the grain size distribution for natural flows may vary significantly. However, the grain size of the gravels used in this study only ranges from 10 to 15 mm (i.e., effective diameter,  $D_e$ , is 12 mm). The narrow range of grain size adopted in this study made it easier to characterize the effective grain diameter (Hsu et al., 2008) for scaling (Equation 9) and to improve the accuracy of the PIV analysis. The PIV technique is less reliable when analyzing the velocity fields of granular flows with particles that cover a wide range of sizes (Sanvitale & Bowman, 2016).

The gate was pneumatically controlled and lifts vertically to simulate dam-break initiation (Stansby et al., 1998). Upon dam-break initiation, the mass of gravel was allowed to accelerate down the rigid bed before flowing on top of the erodible one.

The erodible bed was designed to be 0.17 m in depth to ensure an unlimited supply of the bed material so that all the erosion potential of the flow was utilized. Wang et al. (2013) reported that the particle size distribution of soil may influence the internal friction angle and inter-particle cohesion, which in turn governs the shear strength of the soil bed. Thus, the

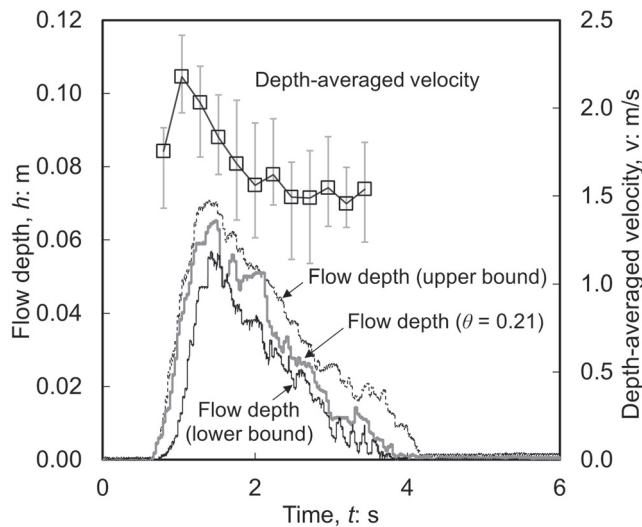


**Figure 4.** Measured flow depth  $h$  and the measured depth-averaged velocity  $v$  just before the flow reaches the erodible bed. The flow depths are measured using an ultrasonic sensor with a sampling rate of 2,000 Hz. The lower and upper bound data series are the minimum and maximum flow depths out of the 13 tests carried out in this study. The depth-averaged velocity is extracted from the images captured by the high-speed camera at the side of the flume using the particle image velocimetry (PIV) technique. The error bars show the range of the velocity at the interface between the non-erodible and erodible beds for all 13 tests.

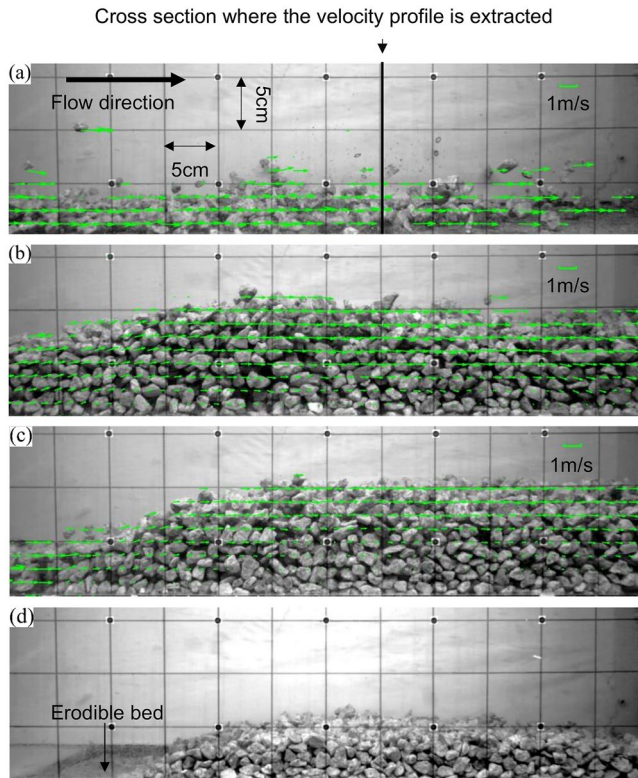


**Figure 5.** Observed flow kinematics captured using the high-speed camera with PIV analysis with a bed volumetric water content  $\theta = 0.22$ . (a)  $t = 0.22$  s, flow front passes the erodible bed; (b)  $t = 1.19$  s, deceleration of the flow; (c)  $t = 2.16$  s, deposition of the flow; (d)  $t = 3.14$  s, final deposited profile. The left edge of the snapshot is the interface between non-erodible and erodible beds. The bottom edge of the snapshot is the initial elevation of the erodible soil bed. A vertical section located 0.35 m downstream from the interface between the non-erodible and erodible beds is used to measure the vertical velocity profile of the flow (shown in Figure 6 below).

camera captured images at a rate of 320 frames per second. An ultrasonic sensor was mounted on top of the channel bed at the interface between the non-erodible and erodible beds to measure the flow depth. The initial matric suction of the soil bed was measured using a tensiometer.

To reveal the erosion depth, 12 erosion columns were installed in the erodible section of the channel (Figure 2d). The erosion columns were essentially threads of washers with inner and outer diameters of 3.1 and 7 mm, respectively. The washers were threaded through rods that were removable from the base of the erodible section. The columns of washers were initially prepared to the same height as the initial elevation of the erodible bed. The soil bed was then prepared. Afterward, the rods were removed without disturbing the washer columns and soil bed. The 12 columns were installed along the centerline of the channel at distances of  $l = 0.04, 0.08, 0.12, 0.16, 0.20, 0.26, 0.32, 0.38, 0.44, 0.50, 0.56,$  and  $0.62$  m from the interface between the non-erodible and erodible beds. During each test, the washers near the surface of the erodible bed were carried away along with the bed material. The erosion depth was deduced by the difference in the height of the columns before and after the test.

### 3.4. Particle Image Velocimetry (PIV) Technique

The PIV technique (Thielicke & Stamhuis, 2014; Willert & Gharib, 1991) has been broadly used to study the kinematics of granular flow (Baker et al., 2016; Jiang & Towhata, 2013; Pudasaini et al., 2007; Sarno et al., 2018). The technique adopts an algorithm that compares two images taken at a known time interval

erodible bed was prepared using sandy soil with negligible clay content, which is a common composition of channel bed deposit observed in the field (Chen & Lee, 2004). Excess clay content would increase inter-particle cohesive forces and capillary stresses, and consequently increase the shear strength of the bed material (Lu & Likos, 2006). The particle size distribution of the bed material is shown in Figure 3. The erodible bed was prepared in 9 separate layers. For each layer, dry sandy soil of the same weight was prepared via the pluviation technique (Raghunandan et al., 2012). Water was then applied to each layer with a handheld water sprayer. The tests were carried out 18 h after the preparation of the erodible bed to ensure a uniform bed water content. The volumetric water content of the erodible bed was varied from 0 to 0.3, corresponding to initial matric suctions from 97.8 to 0.1 kPa. The dry density of the bed material was controlled and only varied by less than 3% for each test.

The flume inclination and the effective grain size of the flow material play important roles in scaling. The flow is required to have a characteristic Savage number  $N_{sav}$  greater than 0.1 to ensure dynamic similarity with collisional debris flow fronts. According to Bagnold (1954), the collisional stresses are proportional to the square of the effective grain size. Also, higher flume inclination results in shallower flow depths (Pouliquen, 1999). Thus, the developed model flows are more collisional with coarser grains and higher channel inclination. Correspondingly, flow material with particle sizes ranging from 10 to 15 mm (an effective grain size of 12 mm) and a flume inclination of  $34^\circ$  were selected based on the aforementioned scaling considerations. Table 1 shows a summary of the test program.

### 3.3. Data Acquisition

A pore pressure transducer was buried in the erodible soil bed at an inclined distance of 0.4 m downstream from the interface between the non-erodible and erodible beds at a depth of 0.12 m for each experiment. A high-speed camera was installed at the side of the flume to capture the flow depth, flow velocity and kinematics of flow-bed interaction. The

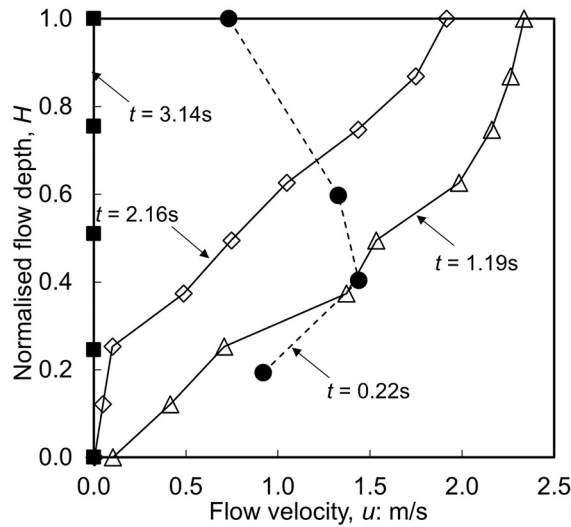


**Figure 6.** Measured vertical velocity profiles at an inclined distance of 0.35 m away from the interface between the non-erodible and erodible beds. Time  $t = 0$  s corresponds to the arrival of the flow front at the interface between the non-erodible and erodible beds. The vertical axis is the flow depth and the horizontal axis is the velocity measured using PIV technique.

(0.003 s in this study) to deduce the instantaneous velocity field. Each image is divided into sub-regions and the cross-correlation functions of each sub-region are calculated to deduce the displacement (White et al., 2003; Willert & Gharib, 1991). The instantaneous velocity field can be deduced by dividing the displacement by the time interval between images. Thus, the shear rate can then be calculated based on the velocity gradient (White et al., 2003; Willert & Gharib, 1991). With reliable estimates of the shear rate, the collisional stresses at the base of the flow can be reliably obtained.

The uncertainty in the PIV measurements mainly stems from any motion blur observed in the captured images and the size of the sub-region selected for analysis. In each test, the shutter speed was set to be 300  $\mu$ s and the speed of the flow is around 1.5 m/s. The estimated maximum motion blur is 0.6 mm, which is only 4% of the effective grain size of the flow particles. Furthermore, Sanvitale and Bowman (2016) assessed the error of the PIV technique in measuring the velocity profile of polydisperse granular flows and demonstrated that PIV analysis can be unreliable if the flow material is highly polydisperse (the uniformity coefficient,  $C_u$ , of the flow material is larger than three). Therefore, the flow material with a narrow grain size range was selected in this study. The size of the sub-region was then set as the effective grain size for the slightly polydisperse flows modeled in this study to minimize the error from image analysis (Sanvitale & Bowman, 2016). The approach proposed by Ashwood and Hungr (2016), whereby a grid was overlaid on two successive images to

estimate the velocity was used to compare and assess the error of the PIV results. The difference between the velocity magnitudes using the approach proposed by Ashwood and Hungr (2016) and PIV is less than 6%.

## 4. Test Results

### 4.1. PIV Analysis, Flow Kinematics and the Erosion Profile

The flow kinematics over the erodible soil bed during each test were captured by the high-speed camera installed at the side of the flume through the clear acrylic sidewall. The flow depth, basal shear rate and the erosion duration can be deduced from high-speed imagery. Based on image analysis with the PIV technique (Thielicke & Stamhuis, 2014; Willert & Gharib, 1991), the Savage number  $N_{Sav}$  and strength normalized collisional stress  $N_{SNCS}$  can be estimated. Table 2 shows a summary of the experimental results including the quantitative description of the flow kinematics and erosion.

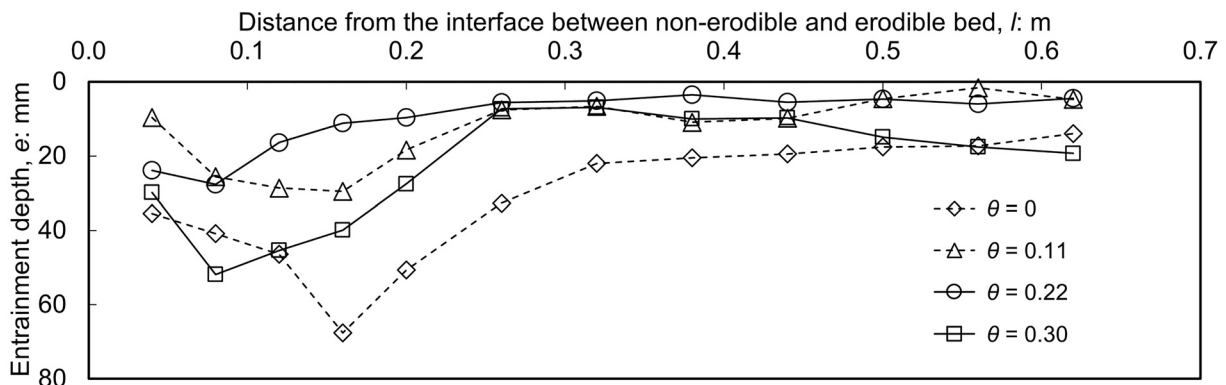


**Figure 7.** Erosion profile measured by the erosion columns (Figure 2d). Four representative curves, representing four of the 13 experiments with different bed volumetric water contents  $\theta$  are shown. A complete set of the erosion depths is shown in Table 3.

**Table 3**  
Summary of Individual Erosion Column Data for Each Test

Volumetric water content, $\theta$	Erosion depth, e, mm												
	$l = 0.04$ m	$l = 0.08$ m	$l = 0.12$ m	$l = 0.16$ m	$l = 0.20$ m	$l = 0.26$ m	$l = 0.32$ m	$l = 0.38$ m	$l = 0.44$ m	$l = 0.50$ m	$l = 0.56$ m	$l = 0.62$ m	
0	35.5	40.9	46.4	67.6	50.7	32.7	22.0	20.5	19.5	17.6	17.3	14.0	
0.06	7.1	31.1	43.0	47.0	51.3	29.5	16.9	7.3	10.7	16.3	16.4	14.0	
0.11	9.6	25.6	28.7	29.5	18.4	7.6	6.6	10.9	9.9	4.6	1.7	4.7	
0.13	17.3	29.6	25.4	19.0	3.8	2.5	4.3	4.6	3.2	3.8	3.6	2.2	
0.16	17.7	18.7	8.4	1.4	1.2	3.4	2.4	2.8	2.6	3.6	2.3	5.3	
0.18	8.2	23.1	32.6	30.4	16.1	8.6	0.3	0.4	0.3	0.3	5.6	1.8	
0.18	18.3	24.1	14.0	2.1	0.7	1.1	3.4	3.1	3.7	7.2	5.0	0.1	
0.20	18.4	24.4	11.9	1.4	1.6	3.9	7.2	5.6	5.5	3.2	1.5	0.1	
0.21	19.2	27.8	17.9	4.1	2.9	4.0	3.6	4.0	6.4	5.0	4.9	3.4	
0.22	23.9	27.7	16.4	11.2	9.7	5.6	5.1	3.5	5.6	4.7	6.0	4.5	
0.24	20.9	35.8	31.0	29.0	7.1	4.0	3.6	7.3	4.6	5.3	4.2	5.0	
0.28	27.6	34.2	46.6	35.4	19.1	7.1	7.7	12.5	11.0	9.0	10.2	5.4	
0.30	29.9	51.9	45.4	39.9	27.5	7.4	6.9	10.0	9.8	14.9	17.6	19.3	

Note.  $l$  represents the distance of each erosion column from the interface between non-erodible and erodible beds.

The Savage number  $N_{sav}$  of the 13 experiments conducted in this study range from 0.28 to 0.49 (Table 2), demonstrating that a collision-dominated flow regime was achieved for the flows modeled. The flow depth obtained from the ultrasonic sensor and the depth-averaged flow velocities extracted from PIV at the interface between the non-erodible and erodible beds are shown in Figure 4. The flow depth increases from 0 to a peak value of 0.58–0.64 m upon the arrival of the flow front. The flow depth increases from 0 to peak values that range from 0.58 to 0.64 m upon the arrival of the flow front. The flow depths eventually decrease to 0 as the supply of gravel from the storage container is depleted. The depth-averaged velocity at the interface between the non-erodible and erodible beds increases from 1.8 m/s to a peak value of 2.2 m/s, and then decreases to a velocity of around 1.5 m/s.

The flow kinematics and the PIV analysis are shown in Figure 5. The arrival of the flow front, where the gravel particles are dispersed, is observed in Figure 5a. Enduring contacts between the gravel particles were not observed. Instead, the gravel particles at the flow front collide with the erodible bed and some bed material was observed to be picked up and eroded. Figure 5b shows the deceleration stage of the flow. In this stage, the flow height gradually increases as the velocity of the gravel particles at the base of the flow gradually decreases. Figure 5c shows the deposition stage, where the velocity of gravels at the bottom layer of the flow decreases to 0 near the downstream end of the erodible section and the gravels eventually deposit. The deposition forms from the bottom layer upwards and toward the upstream direction. Figure 5d shows the final deposition profile.

Velocity profiles were extracted 0.35 m away from the interface between the non-erodible and erodible beds (i.e., in the middle of the erodible bed) from the PIV analysis. The profiles are shown in Figure 6. At  $t = 0.22$  s, the velocity profile is representative of the flow front. At  $t = 1.19$  s, the flow exhibits partial slippage at its base. The flow velocity is around 0.15 m/s at the base and increases to around 2.3 m/s at the surface of the flow. The reciprocal of the slope of each profile represents the shear rate of the flow. It is evident that the shear rate is the highest at the base and gradually decreases with height. At  $t = 2.16$  s, the flow velocity is smaller compared with that measured at  $t = 1.19$  s. The basal flow velocity is nearly zero and the velocity profile of the flowing gravels above the deposited layer is similar to that of a plug flow (Hsu et al., 2008). At  $t = 3.14$  s, deposited gravels are observed and the flow has come to rest.

Figure 7 shows the erosion depth as a function of the distance from the interface between the non-erodible and erodible beds. Generally, erosion increases sharply at the interface. The peak erosion occurs shortly after the interface in the downstream direction. Further downstream, the erosion gradually decreases with inclined distance along the channel. The erosion depth along the downstream half of the erodible section is smaller than that of the upstream half of the section. For the tests carried out in our study, the maximum erosion depth occurs within the first 0.3 m of the erodible bed and nearly 75% of the erosion occurs within the upper half of the erodible bed.

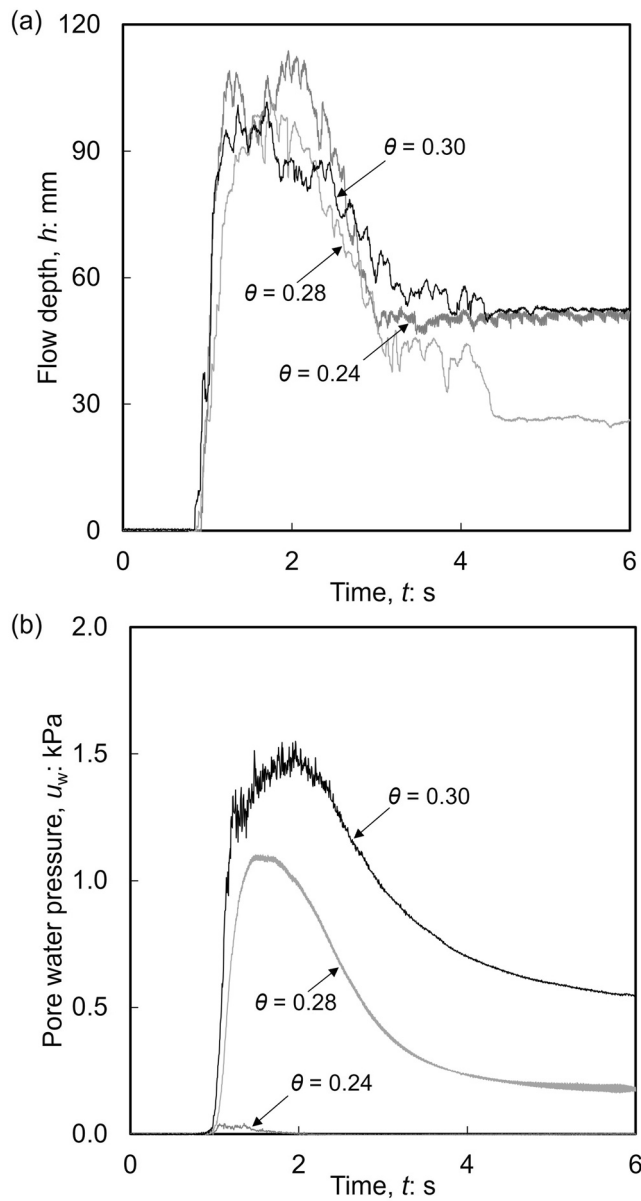


**Figure 8.** Measured time series data. (a) Flow depth; (b) Pore water pressure. The measured time series at the cross-section 0.4 m away from the interface between the non-erodible and erodible beds are shown for three experiments, that is  $\theta = 0.24$ ,  $\theta = 0.28$ , and  $\theta = 0.30$ , where positive pore water pressure was detected. The pore pressure transducer is buried along the centerline of the channel at a depth of 0.12 m in the erodible section.

bed water content due to rainfall. The field data further supports the parabola-like relationship between the average erosion rate and the bed water content.

#### 4.4. Correlation Between Basal Collisional Stresses and Erosion

To characterize the mechanics of erosion of a soil bed by collisional particles, traditional shear-induced erosion theory (Hung et al., 2005; Iverson & Ouyang, 2015) may need to be reconsidered and perhaps supplemented with collision-induced erosion theory proposed in Equation 8. In the flume experiments carried out

#### 4.2. Pore Water Pressure Variation During Erosion

Undrained loading causes an increase in pore pressure in the erodible bed, and the detectable positive pore water pressure was only captured in soil beds with a volumetric water content of 0.24 or higher. Below a water content of 0.24, positive pore water pressure was barely detected (Figure 8). The peak values of the measured positive pore water pressure are extracted from each test, and the corresponding theoretical values are calculated by using Equation 6b. It is evident that the theoretical positive pore water pressure calculated with Equation 6b agrees well with the measured values (Figure 9). The general notion is that there is a critical bed water content around 0.24 where positive pore water pressure is generated when the critical value is exceeded. This observation agrees with Iverson et al. (2011) in that there is a critical bed water content that distinguishes whether positive pore water pressure can be generated in the soil bed or not.

#### 4.3. Correlation Between Matric Suction and Erosion

Figure 10 shows the relationship between the average erosion rate, the shear strength of the soil bed at failure and the initial matric suction. The variation in the average erosion rate with initial matric suction exhibits an inverted left-skewed relationship. The average erosion rate decreases with increasing matric suction until a minimum is reached. Afterward, the average erosion rate increases with the matric suction. It is worthwhile to point out that the variation of the shear strength with the initial matric suction also exhibits a left-skewed relationship. This observation agrees with Equation 2 in that the erosion rate should be inversely related to the bed shear strength.

Iverson et al. (2011) suggests that the average erosion depth increases linearly with the bed water content from the large-scale flume experiments (Figure 11a). However, a linear trend only tells part of the story. More specifically, the erosion depth tends to increase monotonically with the bed water content only when the bed water content is higher than a specific value, as shown by the parabola-like relationship proposed in this study (Figure 11a). By comparing the measured data reported by Iverson et al. (2011), it appears that the reported data may also hint at a potential parabola-like relationship between the average erosion depth and the bed water content (Figure 11a).

To corroborate our findings, a more comprehensive field data set reported by McCoy et al. (2012) can be borrowed to validate the proposed parabola-like relationship between the erosion rate and the bed water content (Figure 11b). The field data were obtained from an observation station at Chalk Cliffs, Colorado, United States from September 2009 to June 2011, when the properties of the bed material were strongly influenced by the

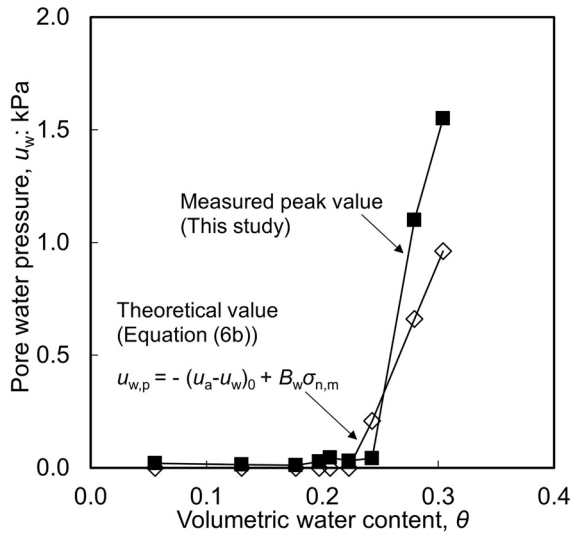


**Figure 9.** The plot of the measured peak positive pore water pressure  $u_{w,p}$  generated in the experiments in this study against the measured initial volumetric water content  $\theta$  of the soil bed material. The theoretical value of the pore water pressure was calculated using Equation 6b.  $(u_a - u_w)_0$  is the initial matric suction of the bed material;  $B_w$  is the pore water pressure parameter and  $\sigma_{n,m}$  is the maximum normal stress calculated with the maximum flow depth. Subscripts  $p$  and  $m$  denote peak and maximum values.

measured by the force plate and reported to be 35, 2, and 14 kPa, respectively, when erosion was detected by the erosion sensor. If the internal friction angle of the bed material is assumed to be  $34^\circ$  (typical value of internal friction angle for soils), then the shear strength calculated for saturated conditions is approximately 22.5 kPa, which is still larger than the measured basal shear stress. This simple back-of-the-envelope

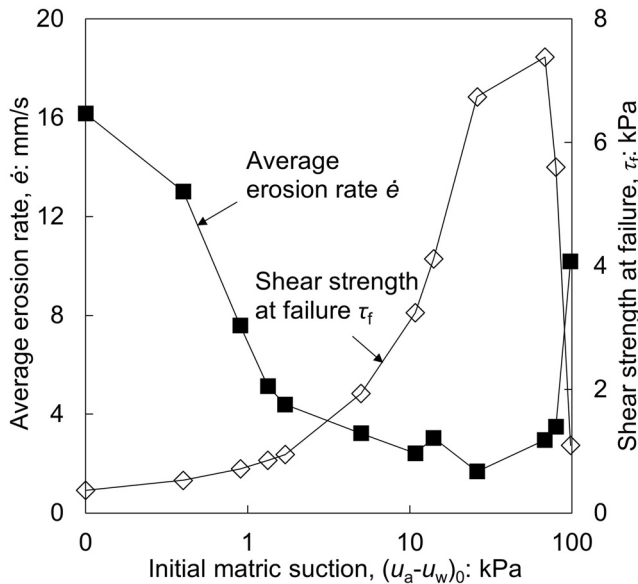


**Figure 10.** The plot of measured erosion rate  $\dot{e}$  and the calculated shear strength of bed material at failure  $\tau_f$  against the measured initial matric suction of the erodible bed  $(u_a - u_w)_0$ . The shear strength at failure  $\tau_f$  is calculated using Equation 7.

in this study, the strength normalized collisional stress  $N_{SNCS}$  can be calculated using Equation 8b with the basic property parameters of the flow and bed material and data extracted from PIV analysis. The experimental data exhibit a positive linear correlation between the average erosion rate  $\dot{e}$  and  $N_{SNCS}$  (Figure 12). This trend shows that the erosion of a soil bed is strongly influenced by the collisional stresses at the base of the flow.

In the flume experiments carried out in this study, the maximum basal shear stress can be estimated as 1.42 kPa based on a flow depth of 0.1 m, which is approximately the maximum flow depth in all tests, and a friction angle of  $43.5^\circ$  for the gravel adopted. Even though the shear strength of the soil bed, with water contents from 0.11 to 0.20, is larger than the estimated maximum shear stress induced by the flow, erosion still occurs. Therefore, traditional shear-induced erosion theory may need to be re-evaluated to consider collisional stresses. Another interesting observation supporting the notion that collisional stresses play an important role in erosion is that the dispersed flow front in the experiments conducted in this study picks up washers and bed material (Figure 5a). Since the dispersed fronts observed from high-speed imagery do not have enduring contacts among the grains, the shear stress imposed on the soil bed can be assumed to be negligible, leaving only collisional stresses to induce failure of the soil bed.

Similar evidence supporting collision-induced erosion was reported based on the field measurements by Berger et al. (2011) at Illgraben, Switzerland. For the debris flow that occurred on the first of July 2008, the basal normal stress, pore water pressure and basal shear stress were measured by the force plate and reported to be 35, 2, and 14 kPa, respectively, when erosion was detected by the erosion sensor. If the internal friction angle of the bed material is assumed to be  $34^\circ$  (typical value of internal friction angle for soils), then the shear strength calculated for saturated conditions is approximately 22.5 kPa, which is still larger than the measured basal shear stress. This simple back-of-the-envelope calculation shows that aside from friction-induced shear stresses, there should be other stresses (i.e., collisional stresses) contributing to the erosion of the soil bed. Another observation that supports the importance of collisional stresses on soil bed erosion is from the field data reported by McArdell et al. (2007) and Berger et al. (2011). The basal shear stress measured by the force plate remains relatively stable during the entire flow process. However, erosion predominantly occurs during the passage of the flow front, where most collisional stresses were reported.

### 5. Discussion

Revealing a critical bed water content that significantly enhances erosion can be advanced using unsaturated soil mechanics. Before a debris flow event, unsaturated soil beds have negative pore water pressures due to capillary effects. If the pore air pressure is assumed to be atmospheric, then the absolute value of the negative pore water pressure is equal to the matric suction, and the pore water pressure decreases with the bed water content. When a debris flow overrides the soil bed, it induces undrained loading and causes the pore water pressure to increase. The increase in pore water pressure is equal to the product of the normal stress and the pore water pressure parameter, which also decreases with the bed water content (Equation 5). Thus, according to Equation 6b, a positive pore water pressure will only be detected when the bed water content exceeds a

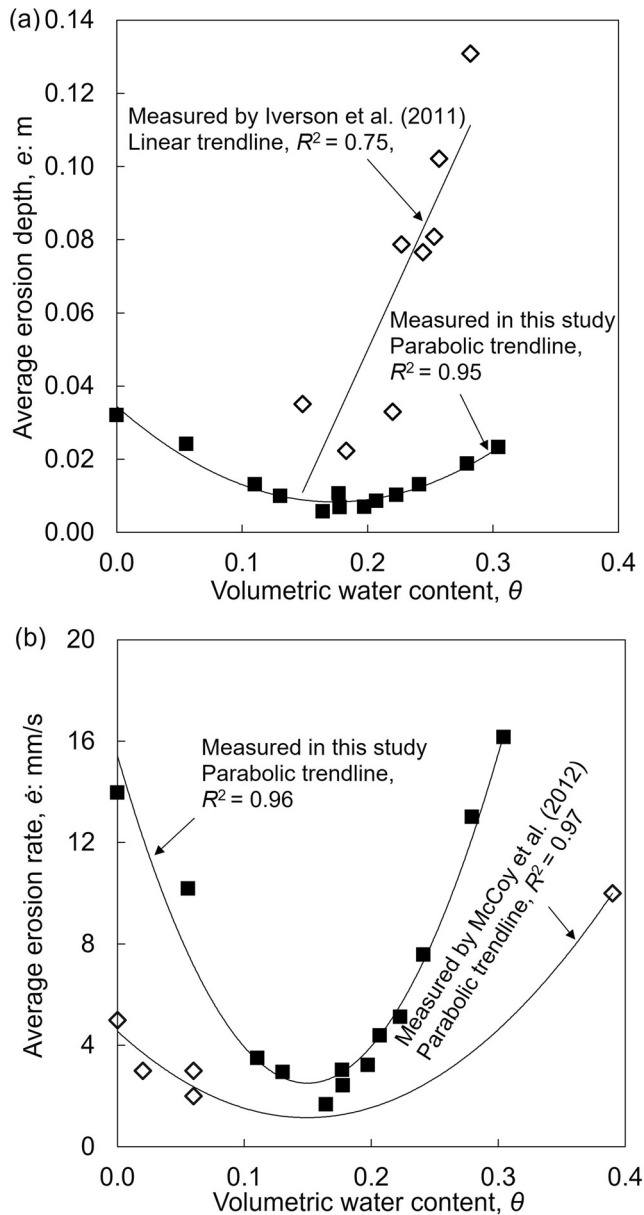


**Figure 11.** Variation of the measured average erosion depth  $e$  (Figure 11a) and measured average erosion rate  $\dot{e}$  (Figure 11b) with the measured volumetric water content of the erodible bed  $\theta$ . The average erosion depth is obtained by taking the average of the erosion depth measured by the 12 erosion columns in each test. The average erosion depth is then divided by the duration of erosion to yield the average erosion rate. The time is estimated by taking the average of the time that erosion occurs at each erosion column based on the high-speed camera videos. Erosion is assumed to cease when the base of the flow reaches a velocity of zero.

critical value, which is when the matric suction of the unsaturated soil bed equals to the pore water pressure increase during undrained loading. Given the importance of capillary stresses, perhaps tensiometers can be used to systematically measure the matric suction of the channel bed soil to improve erosion predictions in high-risk catchments.

The experimental results from this study also show that most erosion occurs near the transition from the non-erodible to the erodible section. A similar spatial erosion pattern was observed by both Haas and Werkom (2016) and Wu et al. (2018). In the experiments carried in this study, the basal collisional stresses calculated with the velocity gradient near the base of the flow do not change much along the whole erodible section. The rather peculiar erosion profile can be attributed to the shielding effects by the deposition layer. The deposition of gravel initially occurs near the downstream end of the erodible bed and propagates toward the upstream direction. The gravels shield the erodible bed from basal collisional stresses. Thus, the soil bed near the interface between the non-erodible and erodible sections experienced a longer timescale for erosion compared to the rest of the bed, and thus, resulted in more erosion.

The findings from this study demonstrate that soil bed erosion may not necessarily increase linearly with the bed water content as demonstrated by Iverson et al. (2011). Instead, erosion exhibits a parabola-like relationship with the bed water content for unsaturated soil beds. Consequently, the parts of channel that are nearly saturated or dry will be more easily eroded because of their low shear strength.

Based on the unique field observation data (Berger et al., 2011), the theory of collision-induced erosion can help to explain the deficiencies of theory relying on purely friction-induced erosion. We know that the magnitude of stresses generated from the interparticle collisions of large boulders can be up to 10 MPa (Okuda et al., 1980), which is expected to exceed the basal frictional shear stress, which typically ranges from 3 to 18 kPa (Berger et al., 2011). Based on this deduction, collisional stresses should be the major contributor to the erosion of soil beds caused by the debris flow front. This finding explains why most erosion occurs mainly during the passage of the flow front (Berger et al., 2011; McCoy et al., 2012), which typically consists of highly collisional boulders. In contrast, insignificant erosion occurs during the passage of the flow body and tail (Berger et al., 2011; McCoy et al., 2012), which have low concentrations of large boulders, and thus, weak collisional stresses (McArdell et al., 2007). Therefore, highly erosive debris flows may develop in channels with boulder-enriched sediments. It is acknowledged that collisional stresses may not be the sole mechanism that drives erosion, but collisional stresses are in fact important and often overlooked. Notwithstanding, based on the current state of research, it remains a scientific challenge to distinguish between the effects of basal collisional stresses and basal shear stress on soil bed erosion. A rigorous erosion model for complex debris flows is perhaps required given the complexity of the mechanics involved in the erosion of a soil bed caused by short-duration point loads.

Modeling of debris flow erosion is a complicated problem that depends on both the dynamic properties of the flow and the water content of the soil bed in a highly non-linear manner. Further compounding the challenges of modeling this problem are the effects of three-dimensional channel geometries and the non-uniform spatial distribution of bed water content (i.e., higher water content along the centerline than further up the banks). A clear and indirect outcome from this study is that there is a pressing need to couple

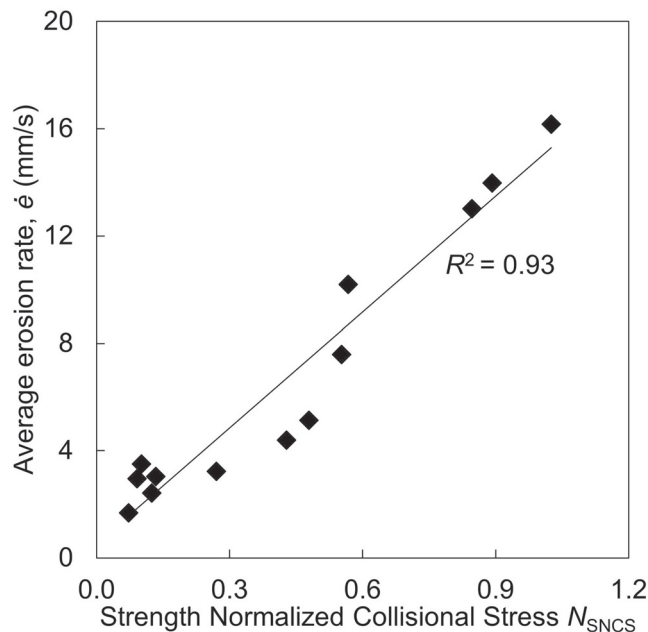


**Figure 12.** The plot of the erosion rate  $\dot{e}$  against the strength normalized collisional stress  $N_{SNCS}$ .  $N_{SNCS}$  is calculated using Equation 8b, where  $v_s$  is the solid fraction of the generated flow,  $\rho_s$  and  $D_c$  are the density and characteristic grain diameter of the solid particles,  $\dot{\gamma}$  is the shear rate,  $\sigma_n$  is the normal stress imposed by the flows,  $B_a$  is the pore air pressure parameter,  $(u_a - u_w)_0$  is the initial matric suction,  $\tan\phi'$  is the effective internal friction angle of the soil and  $\tan\phi^b$  quantifies the effect of matric suction on the shear strength of soil bed.

the hydrological and mechanical effects of soil behavior to advance the current state of debris flow hazard assessment.

Existing erosion models that do not explicitly capture the effects of collisional stresses or unsaturated soil beds are likely gross simplifications of the actual phenomena. These existing models are unlikely to be able to replicate field observations and measurements without extensive calibration. Therefore, jumping directly to the field to calibrate numerical models may not be a reasonable approach. Instead, it may be more sensible to generate high-quality experimental data to bridge the gap between computed results from numerical simulations and field observations. Well-controlled experiments looking at a small subset of variables are perhaps the most favorable for ensuring high fidelity numerical models.

## 6. Conclusions

We interpret the erosion of unsaturated soil beds by debris flows that are dominated by collisional stresses. A new expression that considers both capillary and collisional stresses is proposed. A total of 13 unique physical experiments were carried out to systematically evaluate the proposed theoretical expression. Detailed conclusions may be drawn as follows:

- (1) Contrary to the existing literature, the rate of erosion increases approximately parabolically with the bed water content instead of linearly. This parabola-like relationship is attributed to the nonlinear relationship between the shear strength of unsaturated soil and the bed water content under the influence of capillary effects. This finding implies that the traditional erosion theory may not always yield a conservative estimate of erosion, especially when the bed water content is low.
- (2) Existing work in the literature mainly focuses on basal shear stress as the driving mechanism for soil bed erosion. This study shows that collisional stresses also play a significant role in soil bed erosion, as demonstrated by the positive correlation between the erosion rate  $\dot{e}$  and the strength normalized collisional stress  $N_{SNCS}$ , which is defined as the ratio of the basal collisional stresses to the shear strength of the soil bed. This finding is consistent with hypotheses from field observations and highlights the importance of modeling a flow front with coarse particles to replicate the prototype flow kinematics.
- (3) A critical water content exists for the generation of positive pore water pressure. The critical value corresponds to the water content, at which the initial matric suction of the soil bed equals to the increase in the pore water pressure during undrained loading. When the bed water content is lower than the critical value, positive pore water pressure is barely generated and detectable.
- (4) Modeling of debris flow erosion is a complicated process because of the non-uniform spatial distribution of collisional stresses in a debris flow and the non-linear effects of water content on the shear strength of unsaturated soil. Existing rheological models that do not explicitly consider collisional stresses or unsaturated soil beds are likely gross simplifications of the actual phenomena. This means that there is a pressing need to couple the hydrological and mechanical effects of soil behavior to advance the current state of debris flow hazard assessment. Also, high quality and systematic physical experimental data is essential to bridge the gap between numerical models and field data to ensure high-fidelity predictions of debris flow hazards.

## Data Availability Statement

Some data are cited from two published literatures to support the conclusion. The data are included in these papers (and their supplementary material): McCoy, S. W., Kean, J. W., Coe, J. A., Tucker, G. E., Staley, D. M., & Wasklewicz, T. A. (2012). Sediment entrainment by debris flows: In situ measurements from the headwaters of a steep catchment. *Journal of Geophysical Research: Earth Surface*, 117, F03016. <https://doi.org/10.1029/2012JF002016>

[org/10.1029/2011JF002278](https://doi.org/10.1029/2011JF002278); Iverson, R. M., Reid, M. E., Logan, M., LaHusen, R. G., Godt, J. W., & Griswold, J. P. (2011) Positive feedback and momentum growth during debris-flow entrainment of wet bed sediment. *Nature Geoscience*, 4, 116–121. <https://doi.org/10.1038/NGEO1040>. The experimental data can be accessed with the <https://doi.org/10.25442/hku.14254403>. Datasets for this research are available through: (<https://doi.org/10.25442/hku.14254403>).

### Acknowledgments

The authors are grateful for the generous financial sponsorship from the Research Grants Council of Hong Kong (General Research Funds: 16212618; 16210219; 27205320. Area of Excellence: AoE/E-603/18). Furthermore, the authors thank Mr. Hervé Vicari, who provided the idea pertaining to the erosion column used to measure the erosion depth. His PhD thesis will be published in 2021 from Norwegian University of Science and Technology. The authors declare no financial conflicts of interests.

### References

- Ashwood, W., & Hungr, O. (2016). Estimating total resisting force in flexible barrier impacted by a granular avalanche using physical and numerical modeling. *Canadian Geotechnical Journal*, 53(10), 1700–1717. <https://doi.org/10.1139/cgj-2015-0481>
- Atkinson, J. (2007). *The mechanics of soils and foundations*. CRC Press.
- Bagnold, R. A. (1954). Experiments on a gravity-free dispersion of large solid spheres in a Newtonian fluid under shear. *Proceedings of the Royal Society of London. Series A. Mathematical and Physical Sciences*, 225(1160), 49–63. <https://doi.org/10.1098/rspa.1954.0186>
- Baker, J. L., Barker, T., & Gray, J. M. N. T. (2016). A two-dimensional depth-averaged  $\mu(I)$ -rheology for dense granular avalanches. *Journal of Fluid Mechanics*, 787, 367–395. <https://doi.org/10.1017/jfm.2015.684>
- Berger, C., McArdell, B. W., & Schlunegger, F. (2011). Direct measurement of channel erosion by debris flows, Illgraben, Switzerland. *Journal of Geophysical Research*, 116, F01002. <https://doi.org/10.1029/2010JF001722>
- Bishop, A. W. (1954). The use of pore-pressure coefficients in practice. *Géotechnique*, 4(4), 148–152. <https://doi.org/10.1680/geot.1954.4.4.148>
- Cao, Z., Pender, G., Wallis, S., & Carling, P. (2004). Computational dam-break hydraulics over erodible sediment bed. *Journal of Hydraulic Engineering*, 130(7), 689–703. [https://doi.org/10.1061/\(ASCE\)0733-9429\(2004\)130:7\(689\)](https://doi.org/10.1061/(ASCE)0733-9429(2004)130:7(689))
- Chen, H., & Lee, C. F. (2004). Geohazards of slope mass movement and its prevention in Hong Kong. *Engineering Geology*, 76(1–2), 3–25. <https://doi.org/10.1016/j.enggeo.2004.06.003>
- Estep, J., & Dufek, J. (2012). Substrate effects from force chain dynamics in dense granular flows. *Journal of Geophysical Research*, 117(F1). <https://doi.org/10.1029/2011JF002125>
- Fraccarollo, L., & Capart, H. (2002). Riemann wave description of erosional dam-break flows. *Journal of Fluid Mechanics*, 461, 183–228. <https://doi.org/10.1017/S0022112002008455>
- Fredlund, D. G., & Morgenstern, N. R. (1977). Stress state variables for unsaturated soils. *Journal of the Geotechnical Engineering Division*, 103(ASCE 12919), 447–466. <https://doi.org/10.1061/AJGEB6.000042310.1061/ajgeb6.0000720>
- Fredlund, D. G., Morgenstern, N. R., & Widger, R. A. (1978). The shear strength of unsaturated soils. *Canadian Geotechnical Journal*, 15(3), 313–321. <https://doi.org/10.1139/t78-029>
- Fredlund, D. G., Xing, A., Fredlund, M. D., & Barbour, S. L. (1996). The relationship of the unsaturated soil shear strength to the soil-water characteristic curve. *Canadian Geotechnical Journal*, 33(3), 440–448. <https://doi.org/10.1139/t96-065>
- Froude, M. J., & Petley, D. N. (2018). Global fatal landslide occurrence from 2004 to 2016. *Natural Hazards and Earth System Sciences*, 18(8), 2161–2181. <https://doi.org/10.5194/nhess-18-2161-2018>
- Gan, J. K. M., Fredlund, D. G., & Rahardjo, H. (1988). Determination of the shear strength parameters of an unsaturated soil using the direct shear test. *Canadian Geotechnical Journal*, 25(3), 500–510. <https://doi.org/10.1139/t88-055>
- Haas, T. D., & Woerkom, T. V. (2016). Bed scour by debris flows: Experimental investigation of effects of debris-flow composition. *Earth Surface Processes and Landforms*, 41(13), 1951–1966. <https://doi.org/10.1002/esp.3963>
- Hasan, J. U., & Fredlund, D. G. (1980). Pore pressure parameters for unsaturated soils. *Canadian Geotechnical Journal*, 17(3), 395–404. <https://doi.org/10.1139/t80-046>
- Hilf, J. (1948). Estimating construction pore pressures in rolled earth dams. In *Paper presented at 2nd International Conference on Soil Mechanics and Foundation Engineering*.
- Hsu, L., Dietrich, W. E., & Sklar, L. S. (2008). Experimental study of bedrock erosion by granular flows. *Journal of Geophysical Research*, 113, F02001. <https://doi.org/10.1029/2007JF000778>
- Hsu, L., Dietrich, W. E., & Sklar, L. S. (2014). Mean and fluctuating basal forces generated by granular flows: Laboratory observations in a large vertically rotating drum. *Journal of Geophysical Research: Earth Surface*, 119(6), 1283–1309. <https://doi.org/10.1002/2013JF003078>
- Hung, O., Leroueil, S., & Picarelli, L. (2014). The Varnes classification of landslide types, an update. *Landslides*, 11(2), 167–194. <https://doi.org/10.1007/s10346-013-0436-y>
- Hung, O., McDougall, S., & Bovis, M. (2005). *Debris-flow hazards and related phenomena*. Springer.
- Iverson, R. M. (1997). The physics of debris flows. *Reviews of Geophysics*, 35(3), 245–296. <https://doi.org/10.1029/97RG00426>
- Iverson, R. M. (2012). Elementary theory of bed-sediment entrainment by debris flows and avalanches. *Journal of Geophysical Research*, 117, F03006. <https://doi.org/10.1029/2011JF002189>
- Iverson, R. M., & Ouyang, C. (2015). Entrainment of bed material by Earth-surface mass flows: Review and reformulation of depth-integrated theory. *Reviews of Geophysics*, 53(1), 27–58. <https://doi.org/10.1002/2013RG000447>
- Iverson, R. M., Reid, M. E., Logan, M., LaHusen, R. G., Godt, J. W., & Griswold, J. P. (2011). Positive feedback and momentum growth during debris-flow entrainment of wet bed sediment. *Nature Geoscience*, 4, 116–121. <https://doi.org/10.1038/NGEO1040>
- Jaeger, J. C., Cook, N. G., & Zimmerman, R. (2009). *Fundamentals of rock mechanics*. John Wiley & Sons.
- Jakob, M., Stein, D., & Ulmi, M. (2012). Vulnerability of buildings to debris flow impact. *Natural Hazards*, 60(2), 241–261. <https://doi.org/10.1007/s11069-011-0007-2>
- Jiang, Y.-J., & Towhata, I. (2013). Experimental study of dry granular flow and impact behavior against a rigid retaining wall. *Rock Mechanics and Rock Engineering*, 46(4), 713–729. <https://doi.org/10.1007/s00603-012-0293-3>
- Lu, N. (2008). Is matric suction a stress variable? *Journal of Geotechnical and Geoenvironmental Engineering*, 134(7), 899–905. [https://doi.org/10.1061/\(ASCE\)1090-0241\(2008\)134:7\(899\)](https://doi.org/10.1061/(ASCE)1090-0241(2008)134:7(899))
- Lu, N., & Likos, W. J. (2006). Suction stress characteristic curve for unsaturated soil. *Journal of Geotechnical and Geoenvironmental Engineering*, 132(2), 131–142. [https://doi.org/10.1061/\(ASCE\)1090-0241\(2006\)132:2\(131\)](https://doi.org/10.1061/(ASCE)1090-0241(2006)132:2(131))
- McArdell, B. W., Bartelt, P., & Kowalski, J. (2007). Field observations of basal forces and fluid pore pressure in a debris flow. *Geophysical Research Letters*, 34(7), L07406. <https://doi.org/10.1029/2006GL029183>
- McCoy, S. W., Kean, J. W., Coe, J. A., Tucker, G. E., Staley, D. M., & Wasklewicz, T. A. (2012). Sediment entrainment by debris flows: In situ measurements from the headwaters of a steep catchment. *Journal of Geophysical Research*, 117, F03016. <https://doi.org/10.1029/2011JF002278>

- McDougall, S., & Hungr, O. (2005). Dynamic modeling of entrainment in rapid landslides. *Canadian Geotechnical Journal*, 42(5), 1437–1448. <https://doi.org/10.1139/t05-064>
- Medina, V., Hürlimann, M., & Bateman, A. (2008). Application of FLATModel, a 2D finite volume code, to debris flows in the northeastern part of the Iberian Peninsula. *Landslides*, 5(1), 127–142. <https://doi.org/10.1007/s10346-007-0102-3>
- Okuda, S., Okunishi, K., & Suwa, H. (1980). Observation of debris flow at Kamikamihori Valley of Mt. Yakedade. In *Paper presented at 3rd Meeting of IGU Commission on Field Experiment in Geomorphology*.
- Pirulli, M., & Pastor, M. (2012). Numerical study on the entrainment of bed material into rapid landslides. *Géotechnique*, 62(11), 959–972. <https://doi.org/10.1680/geot.10.p.074>
- Pouliquen, O. (1999). Scaling laws in granular flows down rough inclined planes. *Physics of Fluids*, 11(3), 542–548. <https://doi.org/10.1063/1.869928>
- Pudasaini, S. P., Hutter, K., Hsiau, S.-S., Tai, S.-C., Wang, Y., & Katzenbach, R. (2007). Rapid flow of dry granular materials down inclined chutes impinging on rigid walls. *Physics of Fluids*, 19(5), 053302. <https://doi.org/10.1063/1.2726885>
- Raghunandan, M., Juneja, A., & Hsiung, B. (2012). Preparation of reconstituted sand samples in the laboratory. *International Journal of Geotechnical Engineering*, 6(1), 125–131. <https://doi.org/10.3328/IJGE.2012.06.01.125-131>
- Sanvitale, N., & Bowman, E. T. (2016). Using PIV to measure granular temperature in saturated unsteady polydisperse granular flows. *Granular Matter*, 18(3), 1–12. <https://doi.org/10.1007/s10035-016-0620-6>
- Sarno, L., Carleo, L., Papa, M. N., & Villani, P. (2018). Experimental investigation on the effects of the fixed boundaries in channelized dry granular flows. *Rock Mechanics and Rock Engineering*, 51(1), 203–225. <https://doi.org/10.1007/s00603-017-1311-2>
- Savage, S. B., & Hutter, K. (1989). The motion of a finite mass of granular material down a rough incline. *Journal of Fluid Mechanics*, 199, 177–215. <https://doi.org/10.1017/S0022112089000340>
- Skempton, A. W. (1954). The pore-pressure coefficients A and B. *Géotechnique*, 4(4), 143–147. <https://doi.org/10.1680/geot.1954.4.4.143>
- Sovilla, B., Burlando, P., & Bartelt, P. (2006). Field experiments and numerical modeling of mass entrainment in snow avalanches. *Journal of Geophysical Research*, 111, F03007. <https://doi.org/10.1029/2005JF000391>
- Stansby, P. K., Chegini, A., & Barnes, T. C. D. (1998). The initial stages of dam-break flow. *Journal of Fluid Mechanics*, 374, 407–424. <https://doi.org/10.1017/S0022112098009975>
- Stock, J. D., & Dietrich, W. E. (2006). Erosion of steepland valleys by debris flows. *The Geological Society of America Bulletin*, 118(9–10), 1125–1148. <https://doi.org/10.1130/B25902.1>
- Stock, J., & Dietrich, W. E. (2003). Valley incision by debris flows: Evidence of a topographic signature. *Water Resources Research*, 39(4), ESG1. <https://doi.org/10.1029/2001WR001057>
- Sutherland, A. J. (1967). Proposed mechanism for sediment entrainment by turbulent flows. *Journal of Geophysical Research*, 72(24), 6183–6194. <https://doi.org/10.1029/JZ072i024p06183>
- Takahashi, T. (1978). Mechanical characteristics of debris flow. *Journal of the Hydraulics Division*, 104(8), 1153–1169. <https://doi.org/10.1061/JYCEAJ.0005046>
- Terzaghi, K. V. (1936). The shearing resistance of saturated soils and the angle between the planes of shear. In *Paper presented at 1st International Conference on Soil Mechanics*. Harvard University.
- Thielicke, W., & Stamhuis, E. J. (2014). PIVlab—Toward User-friendly, affordable and accurate digital particle image velocimetry in MATLAB. *Journal of Open Research Software*, 2(1), e30. <https://doi.org/10.5334/jors.bl>
- Vanapalli, S. K., Fredlund, D. G., Pufahl, D. E., & Clifton, A. W. (1996). Model for the prediction of shear strength with respect to soil suction. *Canadian Geotechnical Journal*, 33(3), 379–392. <https://doi.org/10.1139/t96-060>
- Wang, J.-J., Zhang, H.-P., Tang, S.-C., & Liang, Y. (2013). Effects of particle size distribution on shear strength of accumulation soil. *Journal of Geotechnical and Geoenvironmental Engineering*, 139(11), 1994–1997. [https://doi.org/10.1061/\(ASCE\)GT.1943-5606.0000931](https://doi.org/10.1061/(ASCE)GT.1943-5606.0000931)
- White, D. J., Take, W. A., & Bolton, M. D. (2003). Soil deformation measurement using particle image velocimetry (PIV) and photogrammetry. *Géotechnique*, 53(7), 619–631. <https://doi.org/10.1680/geot.2003.53.7.619>
- Willert, C. E., & Gharib, M. (1991). Digital particle image velocimetry. *Experiments in Fluids*, 10(4), 181–193. <https://doi.org/10.1007/bf00190388>
- Wu, Y., Li, P., & Wang, D. (2018). Erosion-deposition regime formation in granular column collapse over an erodible surface. *Physical Review E-Statistical Physics, Plasmas, Fluids, and Related Interdisciplinary Topics*, 98(5), 052909. <https://doi.org/10.1103/PhysRevE.98.052909>
- Yohannes, B., Hsu, L., Dietrich, W. E., & Hill, K. M. (2012). Boundary stresses due to impacts from dry granular flows. *Journal of Geophysical Research*, 117, F02027. <https://doi.org/10.1029/2011JF002150>